# Magnetoabsorption spectra of bilayer graphene ribbons with Bernal stacking

Y. C. Huang,[1] C. P. Chang,[2,3,*] and M. F. Lin[4,3,†]
[1]*Center for General Education, Kao Yuan University, 821 Kaohsiung, Taiwan*
[2]*Center for General Education, Tainan University of Technology, 710 Tainan, Taiwan*
[3]*National Center for Theoretical Sciences, 701 Tainan, Taiwan*
[4]*Department of Physics, National Cheng Kung University, 701 Tainan, Taiwan*
(Received 16 May 2008; revised manuscript received 17 August 2008; published 22 September 2008)

Magnetoabsorption spectra of bilayer graphene ribbons with Bernal stacking are studied by the Peierls-coupling tight-binding method. When the magnetic confinement prevails over the quantum confinement, low-energy spectra chiefly exhibit many Landau peaks, which are strongly modified by the inter-ribbon interactions and the magnetic-field magnitude ($B$). The spectra show denser Landau peaks in bilayer graphene ribbon than in a monolayer ribbon with the same ribbon width. The absorption frequencies of Landau peaks of a wide monolayer ribbon show the $\sqrt{B}$ dependence, while those of a bilayer ribbon exhibit a varying $B$-field dependence. In the spectra region $\omega \leq 100$ meV, the absorption frequencies of Landau peaks are linearly dependent on the magnetic-field magnitude. At $\omega \geq 100$ meV, they evolve from the $B$ dependence to the $\sqrt{B}$ dependence with the increase in the field strength. The absorption frequencies of Landau peaks exhibit $\sqrt{B}$ dependence at $B \geq 20$ T. The relationship between the magneto-optical properties and electronic structures (the state energies and wave functions) are explored. The Landau wave functions are illustrated and used to identify the optical selection rule.

DOI: 10.1103/PhysRevB.78.115422 PACS number(s): 73.20.At, 73.61.−r

## I. INTRODUCTION

Recently, the observation of two-dimensional (2D) graphene and few-layer graphene[1–4] has triggered many experimental and theoretical studies. The nanoscale graphene is expected to be a potential candidate for the next-generation electronics simply because of its ballistic transport at room temperature and mechanical stability. Progress in academic research would help explore possible applications and design options. Experimental and theoretical studies show that graphene, a planar hexagonal lattice of carbon atom, exhibits many interesting properties, such as the two linear bands intersecting at the Fermi energy,[5,6] the novel quantum Hall effect,[7–9] and the electric-field-induced carrier transition.[1] Few-layer graphenes are the stack of graphene layers. Their intriguing electronic properties emerge through the change in layer number, the alternation of stack ordering, and the application of external field.[10–12] Among them, the bilayer graphene with Bernal stacking (the AB-stacked bilayer graphene) has aroused the most studies. Because of the interlayer interactions and geometrical structure, the Bernal bilayer graphene exhibits four branches of the energy curves. Each curve is made of parabolic bands and sublinear bands.[10–13] Bilayer graphene is a two-dimensional semimetal with the tiny overlap between the highest occupied valence band and the lowest unoccupied conduction band. By opening a tunable energy gap, the application of a perpendicular electric field can induce the semimetal-semiconductor transition.[11–15] Such interesting properties might offer an alternative design option for the electronic devices.

The difference in essential properties between the monolayer and bilayer graphenes is also revealed in transport. Experimentally, a monolayer graphene shows the Berry's phase $\pi$ and the half-integer quantum Hall effect.[8] On the other hand, the integer quantum Hall effect, accompanied by Berry's phase of $2\pi$, arises in bilayer graphene.[7] The above-mentioned data might be attributed to the difference in magnetic bands. In the absence of the magnetic field, charge carriers in a monolayer graphene are characterized by a linear dispersion, while those in bilayer graphene have a parabolic energy spectrum. The low-energy Landau levels (LLs) of a monolayer graphene subjected to a perpendicular magnetic field are well described by the effective-mass model. They follow the simple relation $|E| \sim \sqrt{B|n|}$, where $B$ is the magnetic-field strength and $n$ is the subband index. The effective-mass model is extended to conveniently study the magnetoelectronic properties of a bilayer Bernal graphene in the presence of a perpendicular magnetic field.[16–18] Bilayer graphene shows more complicated LLs, whose energies are dramatically modified by the interlayer interactions. This model predicts that the energies of LLs, which are very close to $E_F$, are approximately proportional to $\sqrt{n(n-1)B}$ when some interlayer interactions are excluded for the calculation simplicity. However, the effective-mass model is only suitable for the low-energy LLs, meaning that this model cannot offer the physical pictures in the overall energy region.

Peierls-coupling tight-binding method is an alternative option used to study the full magnetic band of graphitic systems.[19–24] It has been utilized to explore the magnetoabsorption spectra of a monolayer graphene.[21] By diagonalizing a $2q \times 2q$ complex Hamiltonian matrix, where $q$ is the inverse of the magnetic flux $\phi$, the full magnetic band and the related wave functions are obtained to calculate the absorption spectra. This method will be met with a serious obstacle when we consider the magnetoelectronic properties at a low magnetic field. For example, one needs to diagonalize a $160\,000 \times 160\,000$ complex matrix at $B=1$ T. An efficient numerical method is proposed to overcome this problem.[25] The arrangement of matrix elements in the band storage allows us to easily diagonalize such a high rank ma-

 ©2008 The American Physical Society

trix. This method is successfully used to study the magnetoelectronic properties, such as state energies and Landau wave functions, of the AB-stacked bilayer graphene. However, it is not suitable to calculate the magneto-optical properties of the AB-stacked bilayer graphene due to the labor numerical task in calculating the velocity matrix element.[21] Thus, another way to efficiently calculate the magneto-optical properties of bilayer graphene is inspired.

Peierls-coupling tight-binding method has been employed to study the magnetoelectronic properties and absorption spectra of monolayer graphene zigzag ribbons with the ribbon width changing from the nanometer to the mesoscopic scale.[26] The magnetic bands and the related wave functions of a ribbon are dominated by the magnetic confinement and quantum confinement.[26–28] When the ribbon width is wider than the spatial extent of Landau wave functions, the Landau states exist.[26] As a result, the magnetoabsorption spectra exhibit sharp Landau peaks. The spectral frequencies of Landau peaks are chiefly determined by the field strength. The peak height runs higher with the increase in the ribbon width. The results show that at a low magnetic field, the magnetoelectronic properties of a ribbon with sufficient width are deduced to be the same as those of a 2D graphene.

We now use the tight-binding method to study the magnetoabsorption spectra of bilayer graphene ribbons with Bernal stacking. There are several advantages to this method: (i) Hamiltonian representation of the zigzag ribbon is a real Hermitian matrix in the band storage. The state energies and the wave functions are efficiently obtained by the diagonalization of such a band-storage matrix. (ii) The Peierls-coupling tight-binding method is able to provide the full-band electronic structure.[26] (iii) This method is easy to include the interlayer interactions and is applied to multilayer systems, e.g., bilayer, trilayer, and four-layer graphene ribbons.

This paper is organized as follows: Section II discusses the Hamiltonian matrix elements of a bilayer graphene ribbon in the presence of a perpendicular magnetic field. Then, magnetoelectronic and optical properties are explored in Sec. III. Finally, conclusion remarks are drawn in Sec. IV. Most importantly, the studies are helpful to understanding the magnetic-optical properties of a bilayer Bernal graphene.

## II. THEORY

An $N_y$ AB-stacked bilayer zigzag graphene ribbon, as illustrated in Fig. 1, is the pile of two identical monolayer zigzag ribbons with Bernal stacking. Each ribbon has $N_y$ zigzag lines along the $y$ axis. Hydrogen atoms are attached to carbon atoms located at cusps of the outmost zigzag lines. (For details see Ref. 26.) Along the $z$ axis, atoms $A_m^2$ lie directly on top of atoms $A_m^1$ while the projections of atoms $B_m^2$ are in the center of the hexagonal rings on the lower ribbon plane. $A_m^1$ and $B_m^1$ ($A_m^2$ and $B_m^2$) denote atoms $A$ and $B$ in the $m$th zigzag line on the lower (upper) ribbon plane. The inter-ribbon distance is $l_c$=3.35 Å and C-C bond length is $b$=1.42 Å.[29] The lattice periodicity along the $x$ axis is $l_x=\sqrt{3}b$ and the first Brillouin zone is defined by $-\pi/l_x \le k_x \le \pi/l_x$. An AB-stacked bilayer zigzag ribbon has $4N_y$ atoms

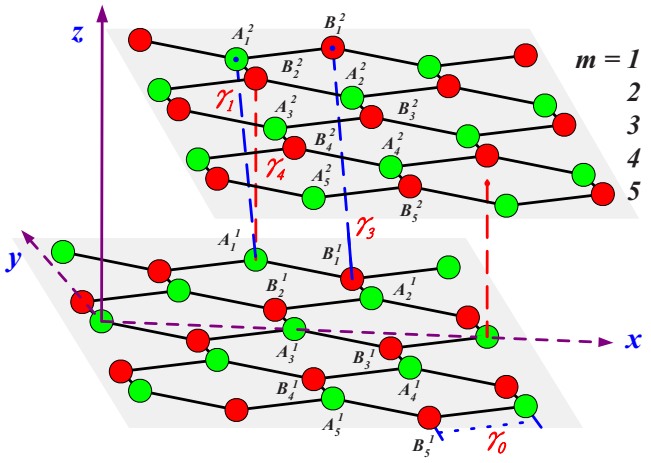


FIG. 1. (Color online) The geometrical structure and the atom-atom interactions $\gamma_i$ of bilayer zigzag ribbon. $\gamma_0$ is the in-plane hopping. $\gamma_1$ is the inter-ribbon interaction between two atoms $A_m^1$ and $A_m^2$. The inter-ribbon hopping between atoms $B_m^1$ and $B_m^2$ is $\gamma_3$. $\gamma_4$ represents the interaction between atoms $A_m^1$ and $B_m^2$ ($A_m^2$ and $B_m^1$).

in a 2D primitive cell. Each atom contributes one $2p_z$ orbital to the $\pi$-electronic structure. That is, only the $2p_z$ orbitals of the carbon atoms are taken into consideration.[26,30,31]

In the presence of a perpendicular magnetic field $\mathbf{B}=(0,0,B)$, through the Peierls substitution, Hamiltonian of the AB-stacked bilayer graphene ribbon is $\mathbf{H}=\Sigma_i \epsilon_{p,i} + \Sigma_{i,j}(\gamma_{i,j} e^{i2\pi\theta_{i,j}} c_i^+ c_j + \text{H.c.})$, where the site energy $\epsilon_p$ is set to zero. $\theta_{i,j}$ is Peierls phase shift induced by the magnetic field. $c_i^+(c_j)$ is the creation (annihilation) operator at the $i$th ($j$th) site. The definition of the tight-binding parameters $\gamma_{i,j}$ is shown in Fig. 1. The different chemical environment between atom $A$ and atom $B$ is reflected in the site energy $\gamma_6$. The values of atom-atom interactions are as follows:[29] $\gamma_0$ =2.598 eV, $\gamma_1$=0.364 eV, $\gamma_3$=0.319 eV, $\gamma_4$=0.177 eV, and $\gamma_6$=−0.026 eV. The vector potential with the Landau gauge $\mathbf{A}=(-By,0,0)$ is picked out. The benefit of such a choice is to preserve the translation invariance along the $x$ axis. Thus, there are $4N_y$ atoms in a primitive cell found. The tight-binding Bloch function could be expressed as

$$|\Phi(k_x,y)\rangle = \sum_{m=1}^{N_y} a_{A_m^1}|A_m^1\rangle + b_{B_m^1}|B_m^1\rangle + a_{A_m^2}|A_m^2\rangle + b_{B_m^2}|B_m^2\rangle, \tag{1}$$

where $|A_m^1\rangle$, $|B_m^1\rangle$, $|A_m^2\rangle$, and $|B_m^2\rangle$ are the linear superposition of the $2p_z$ orbitals from the periodic $A_m^1$, $B_m^1$, $A_m^2$, and $B_m^2$ carbon atoms. $a_{A_m^1}$, $b_{B_m^1}$, $a_{A_m^2}$, and $b_{B_m^2}$ are the site amplitudes. The $4N_y \times 4N_y$ Hamiltonian representation is a band-storage matrix with the nonzero elements $h_{m,m}$, $h_{m,m+1}$, and $h_{m+1,m}$, where $h_{m,m}$, $h_{m,m+1}$, and $h_{m+1,m}$ are $4\times4$ block matrices. Matrix elements of the upper triangular part of the Hermitian matrix $h_{m,m}$, spanned by four Bloch functions $|A_m^1\rangle$, $|B_m^1\rangle$, $|A_m^2\rangle$ and $|B_m^2\rangle$, are expressed as follows:

$$
\begin{aligned}
h_{m,m}(1,1) &= \gamma_6, \\
h_{m,m}(1,2) &= 2\gamma_0 \cos\{k_x I_x - \pi(m-[N])\phi\}, \\
h_{m,m}(1,3) &= \gamma_1, \\
h_{m,m}(1,4) &= 2\gamma_4 \cos\left\{k_x I_x - \pi\left(m-[N]-\frac{1}{3}\right)\phi\right\}, \\
h_{m,m}(2,2) &= 0, \\
h_{m,m}(2,3) &= 2\gamma_4 \cos\{k_x I_x - \pi(m-[N])\phi\}, \\
h_{m,m}(2,4) &= \gamma_3, \\
h_{m,m}(3,3) &= \gamma_6, \\
h_{m,m}(3,4) &= 2\gamma_0 \cos\left\{k_x I_x - \pi\left(m-[N]-\frac{1}{3}\right)\phi\right\}, \\
h_{m,m}(4,4) &= 0,
\end{aligned}
\tag{2}
$$

where the term $[N]=(N_y+1)/2$ is used to locate the origin of coordinate in the center of the lower ribbon plane. Magnetic flux passing a hexagonal ring induces the Peierls phase shift $2\pi\phi$. The term $\pi\phi/3$ in Eq. (2) results from the difference between the centers of the two ribbons. The off-diagonal block matrices $h_{m,m+1}$ and $h_{m+1,m}$ satisfy the relation $h_{m,m+1}=h_{m+1,m}$. The nonzero matrix elements of matrix $h_{m,m+1}$ are

$$
\begin{aligned}
h_{m,m+1}(1,4) &= \gamma_4, \\
h_{m,m+1}(2,1) &= \gamma_0, \\
h_{m,m+1}(2,3) &= \gamma_4, \\
h_{m,m+1}(2,4) &= 2\gamma_3 \cos\left\{k_x I_x - \pi\left(m-[N]+\frac{1}{3}\right)\phi\right\}, \\
h_{m,m+1}(3,4) &= \gamma_0.
\end{aligned}
\tag{3}
$$

By diagonalizing the Hamiltonian matrix, we obtained eigenvalues and eigenvectors. Eigenvalues are the energy dispersions $E^{c,v}(k_x I_x)$ in unit of $\gamma_0$, where $c$ ($v$) represents the unoccupied (occupied) states. The eigenvector $|\cdots, a_m^{c,v}, b_m^{c,v}, a_m^{c,v}, b_m^{c,v}, \cdots\rangle$ is the envelope function $|\Psi^{c,v}(y)\rangle$ along the $y$ direction.

## III. MAGNETOELECTRONIC AND OPTICAL PROPERTIES

The low-energy magnetic bands of the $N_y=3000$ monolayer zigzag ribbon at $B=20$ T, as shown in Fig. 2(a), exhibits both the Landau levels and the additional spectrum.[32,33] Still, we focus only on the Landau levels here. $E^c$ are symmetric to $E^v$ about $E_F=0$. The state energy of

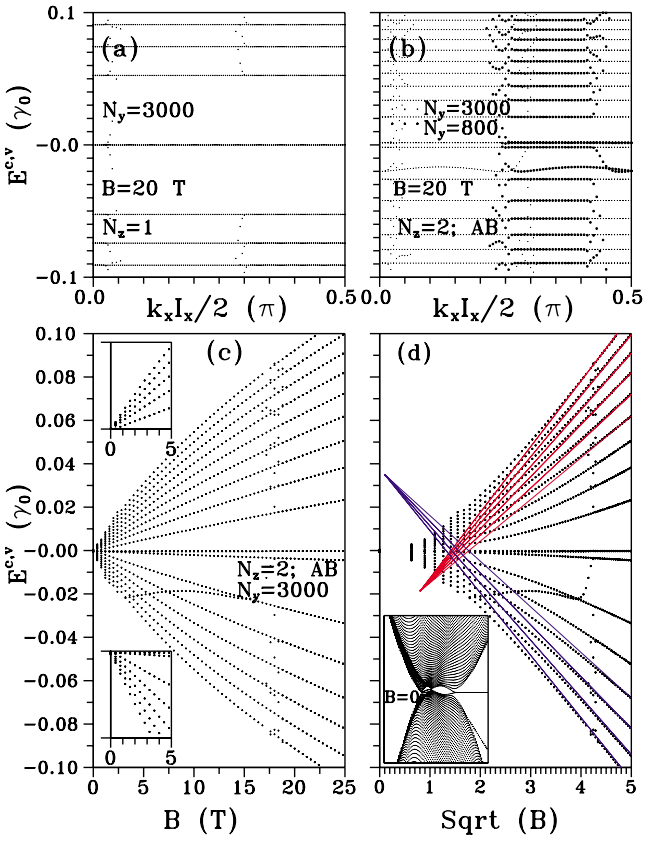


FIG. 2. (Color online) (a) and (b), respectively, show the low-energy magnetic bands of the $N_y=3000$ monolayer and bilayer ribbons at $B=20$ T. (c) Landau plot of the $N_y=3000$ bilayer ribbon. (d) The relation between the low-energy Landau levels of the $N_y=3000$ bilayer ribbon and $\sqrt{B}$. The inset of (d) exhibits the low-energy dispersions at $B=0$.

Landau subband indexed by $n$ follows the relation $|E| \propto \sqrt{|n|B}$.[26] The highest occupied Landau states and the lowest unoccupied Landau states are degenerate at $E_F$. As a result of the interlayer interactions, the low-energy magnetic bands of the $N_y=3000$ bilayer graphene ribbon exhibits more Landau levels at $B=20$ T [Fig. 2(b)]. The unoccupied states (the occupied states) away from $E_F$ are characterized by $E_{\tilde{n}}^c(E_{\tilde{n}'}^v)$ with the subband index $\tilde{n}=0,1,2,3,\cdots(\tilde{n}'=0,-1,-2,-3,\cdots)$. $E_{\tilde{n}}^c$ is asymmetric to $E_{\tilde{n}'}^v$ about $E_F=0$. The Landau-level degeneracy at $E=0$ is lifted and there exists an energy gap $E_g=E_{\tilde{n}=0}^c-E_{\tilde{n}'=0}^v$. In short, the inter-ribbon interactions generate new Landau levels, change the state energies of Landau levels, lift the degeneracy, alter the energy spacings, destroy the symmetry between $E^c$ and $E^v$, and induce an energy gap $E_g$. Notably, the Landau-level energies are independent of the ribbon width, $N_y=800$ [the heavy dots in Fig. 2(d)], for example. That is, they are the same as those of a bilayer graphene.

The magnetoelectronic properties of graphene ribbons are chiefly dominated by the competition between the ribbon width and the spatial distribution of Landau wave function.[27] Nemec *et al.*[24] show that as the ribbon width is narrower than the critical width $w_{\text{critical}}=\sqrt{8\pi}l_B$, where $l_B=\sqrt{\frac{\hbar}{eB}}$ is the magnetic length, the Landau levels of a graphene ribbon disap-

pear and the magnetic bands will differ from the Landau levels (flatbands) of an infinite graphene system.[17] The results of the study are consistent with those of Nemec. At **B** =20 T, the $n=1$ Landau level of a monolayer or bilayer graphene ribbon emerges as the ribbon width $w$ is wider than a critical width $w_{\text{critical}} \approx 4.4 l_B$ (or $N_y \geq 124$).[26] Within this critical width, the Landau wave functions touch the ribbon edges and the Landau level does not exist. As a result, the Hall-edge states emerge, which are clearly distinguished from the Landau levels of an infinite graphene system.

Compared with the simple square-root-of-$B$ dependence of a monolayer ribbon,[26] the bilayer ribbon shows a more complicated Landau plot, the Landau-level energies vs the field strength. The calculation results show that Landau-level energies $E_{\tilde{n}}^{c}(E_{\tilde{n}'}^{v})$ with $\tilde{n}<2(|\tilde{n}'|<2)$ grow linearly at $B \leq 25$ T [Fig. 2(c)]. Thus, the increase in magnetic-field strength enhances the energy gap $E_g = E_{\tilde{n}=0}^{c} - E_{\tilde{n}=0}^{v}$. The gap is closed at $B=0$ because the bilayer system is a semimetal with the tiny overlap of the highest valence and the lowest conduction bands [the inset of Fig. 2(d)]. The magnetic field cannot induce a band gap, i.e., $E_g=0$, in a monolayer graphene. Such a result means that with the close of chemical difference ($\gamma_6$), and interlayer interactions ($\gamma_1, \gamma_3, \gamma_4$), $E_g$ of a bilayer ribbon is equal to zero for any magnetic field. The nonzero energy gap of this bilayer system is caused by the cooperation of the magnetic field, chemical difference, and interlayer interactions. On the other hand, $E_{\tilde{n}}^{c}(E_{\tilde{n}'}^{v})$ with $\tilde{n} \geq 2(|\tilde{n}'| \geq 2)$ exhibit different behavior. First, they obey the relation $E \propto B$ at $B \leq 5$ T [Fig. 2(c)], characteristic of the massive electrons (holes), yet such a characteristic disappears with the increase in the field strength. At $B \geq 5$ T, the Landau plots deviate from the linear-in-$B$ dependence. Figure 2(d) exhibits the Landau-level energies vs $\sqrt{B}$. In the presence of a strong field, the tangent lines of the curves pass through the same point $\Delta$. Landau-level energies follow the simple relation $E_{\tilde{n}}^{c}(E_{\tilde{n}'}^{v}) \propto \sqrt{B}$. The electrons feature the massless carriers.

The dependence of the Landau-level energies on the subband index $\tilde{n}(|\tilde{n}'|)$ and the field strength is critically determined by the Landau-level energies. In the energy region $|E|<0.02\gamma_0 \simeq 50$ meV, the Landau plots indexed by $\tilde{n} \geq 2(|\tilde{n}'| \geq 2)$ exhibit the linear-in-$B$ dependence at $B \leq 5$ T. Then, they evolved from a pure linear $B$ dependence to a square-root $B$ dependence with the increase in the field strength within the energy region $0.02\gamma_0 < |E| < 0.04\gamma_0$, and finally they exhibit the linear-in-$\sqrt{B}$ dependence at $B \geq 16$ T. The result predicted by the Peierls-coupling tight-binding method is in agreement with that of the experimental measurement.[34] Moreover, as shown in the insets of Fig. 2(c), the low lying Landau levels within the energy region $|E|<0.02\gamma_0 \simeq 50$ meV follow the relation $|E| \propto |\tilde{n}|$B, which is consistent with the predicted result of the effective-mass model.[16]

The characteristics of Landau wave functions $\Phi_{\tilde{n}}(k_x, y)$ [Eq. (1)] are revealed in the envelope function $\Psi_{\tilde{n}}(y)$. Landau wave functions at $k_x=\pi/3$ of the $N_y=3000$ bilayer ribbon subjected to several different magnetic-field magnitudes are investigated. The main feature of $\Psi_{\tilde{n}}(y)$ is independent of the magnetic-field magnitude. Thus, Landau wave functions

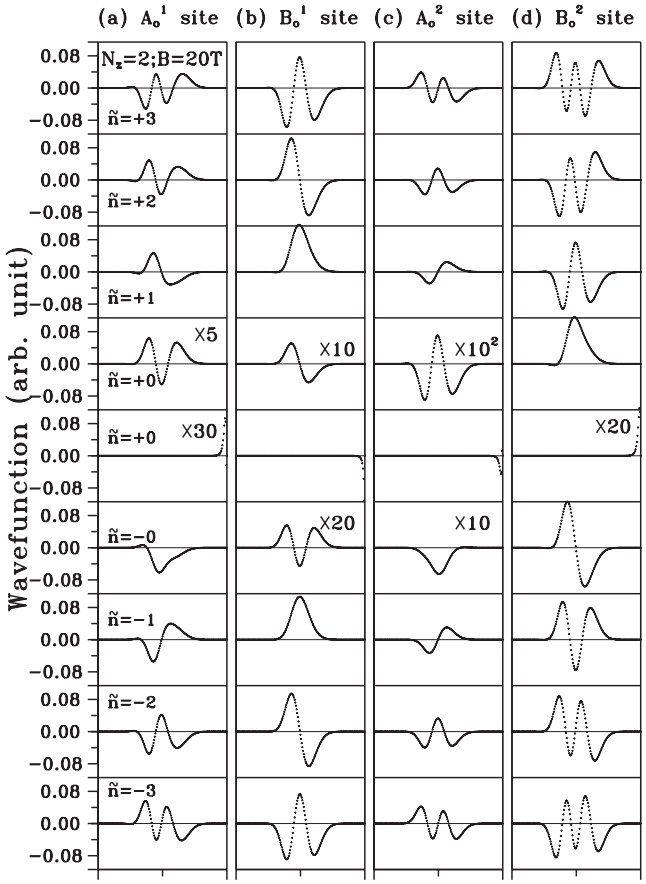


FIG. 3. The envelope functions at $k_x I_x = \pi/3$ and $B=20$ T related to the unoccupied (occupied) Landau levels indexed by $\tilde{n}=0$, 1, 2, and 3 ($\tilde{n}=0, -1, -2$, and $-3$). (a), (b), (c), and (d), respectively, illustrate the subenvelope functions $\psi(A_o^1)$, $\psi(B_o^1)$, $\psi(A_o^2)$, and $\psi(A_o^2)$. $A_o^1$ or $B_o^1$ ($A_o^2$ or $B_o^2$) represent $A$ or $B$ atoms located at the *odd* zigzag lines at the lower (upper) ribbon plane.

$\Phi_{\tilde{n}}(k_x, y)$ at $B=20$ T are chosen as a model for further study. $\Psi_{\tilde{n}}(y)$ with $\tilde{n} \leq 3$ ($|\tilde{n}'| \leq 3$) are shown in Fig. 3. The interesting characteristics of each $\Psi_n(y)$ emerged through the decomposition of $\Psi_n(y)$ into eight subenvelope functions. $\Psi_n(y)$ is rewritten as

$$\Psi_{\tilde{n}}^{c,v} = \psi^{c,v}(A_o^1) + \psi^{c,v}(B_o^1) + \psi^{c,v}(A_e^1) + \psi^{c,v}(B_e^1) + \psi^{c,v}(A_o^2) + \psi^{c,v}(B_o^2) + \psi^{c,v}(A_e^2) + \psi^{c,v}(B_e^2), \quad (4)$$

where $A_o^1$, $A_e^1$, $B_o^1$, and $B_e^1$ ($A_o^2$, $A_e^2$, $B_o^2$, and $B_e^2$) represent $A$ or $B$ atoms located at the *odd* or *even* zigzag lines at the lower (upper) ribbon plane. For example, the subenvelope function $\psi(A_o^1)$ is $|a_{A_1^1}, a_{A_3^1}, \cdots, a_{A_m^1}, \cdots\rangle$, where $m$ is an odd number. Only four subenvelope functions, $\psi^{c,v}(A_o^1)$, $\psi^{c,v}(B_o^1)$, $\psi^{c,v}(A_o^2)$, and $\psi^{c,v}(B_o^2)$, are displayed in Fig. 3 because $\psi^{c,v}(A_o^1) = -\psi^{c,v}(A_e^1)$, $\psi^{c,v}(B_o^1) = -\psi^{c,v}(B_e^1)$, $\psi^{c,v}(A_o^2) = -\psi^{c,v}(A_e^2)$, and $\psi^{c,v}(B_o^2) = -\psi^{c,v}(B_e^2)$. As illustrated, the Landau wave functions related to the double degenerate $E_{\tilde{n}=0}^{c}$ state are different. The subenvelope function $\psi^{c}(B_o^1)$ [$\psi^{c}(A_o^2)$] of $\Psi_{\tilde{n}=0}^{c}$ is strongly confined at one of the zigzag edges of the lower (upper) ribbon. It is a specially localized state located nearby at the ribbon edges. Except the specially localized state, the

shape of the envelope function $\Psi^{c,v}_{\tilde{n}}$ is very sensitive to the Landau-level energy or the subband index. $\Psi^{c}_{\tilde{n}=0}$ ($\Psi^{v}_{\tilde{n}'=0}$), the envelope function of the lowest unoccupied LL (the envelope function of the highest unoccupied LL), is chiefly dominated by the subenvelope function $\psi^{f}(B^2_o)$ [$\psi^{p}(B^2_o)$]. The site amplitude of $B^2$ atoms at the upper ribbon is much larger than others. Away from $E_F$, the LL wave functions are determined by both $\psi(B^1_o)$ and $\psi(B^2_o)$, the site amplitudes of the $B$ atoms in the lower and upper ribbons. $\psi(B^1_o)$ and $\psi(B^2_o)$ have almost the same contribution to the Landau wave function.

The subenvelope functions belong to the localized states, and they also show the oscillating behavior in the confined region. The site amplitude changes signs at the nodes. The number of nodes characterizes the spatial symmetry of the Landau wave function. That is, each subenvelope function of Landau wave function can be specifically described by the number of nodes, which is closely related to the Landau-level energy. Thus, the subband index is used as a quantum number to label the Landau wave function. Envelope function $\Psi^{c}_{\tilde{n}}$ indexed by $|\tilde{n}| \geq 2$ is denoted as follows:

$$\Psi^{c}_{\tilde{n}} = \psi_{\tilde{n}}(A^1_o) - \psi_{\tilde{n}}(A^1_e) + \psi_{\tilde{n}-1}(B^1_o) - \psi_{\tilde{n}-1}(B^1_e) + \psi_{\tilde{n}}(A^2_o) - \psi_{\tilde{n}}(A^2_e) + \psi_{\tilde{n}+1}(B^2_o) - \psi_{\tilde{n}+1}(B^2_e), \quad (5)$$

where the subscript of the subenvelope function $\psi$ labels the number of nodes. Each subenvelope function has its own spatial symmetry. Both $\psi_{\tilde{n}}(A^1_o)$ and $\psi_{\tilde{n}}(A^2_e)$ have $\tilde{n}$ nodes. On the other hand, $\psi_{\tilde{n}-1}(B^1_o)[\psi_{\tilde{n}+1}(B^2_e)]$ has $\tilde{n}-1(\tilde{n}+1)$ nodes. The envelope function $\Psi^{c}_{\tilde{n}=3}$, for instance, reads

$$\Psi_{\tilde{n}=3} = \psi_3(A^1_o) - \psi_3(A^1_e) + \psi_2(B^1_o) - \psi_2(B^1_e) + \psi_3(A^2_o) - \psi_3(A^2_e) + \psi_4(B^2_o) - \psi_4(B^2_e). \quad (6)$$

The envelope functions $\Psi^{v}_{\tilde{n}'=-3}$ and $\Psi^{c}_{\tilde{n}=3}$ have similar subenvelope functions. Due to the orthogonality of wave function, $\Psi^{v}_{\tilde{n}'=-3}$ and $\Psi^{c}_{\tilde{n}=3}$ are different from each other in the sign of some of the subenvelope functions. Notably, the highest occupied and lowest unoccupied LLs have their own spatial symmetry or oscillating behavior. The number of nodes corresponding to the subenvelope functions $\psi^{f}(A^1_o)$, $\psi^{f}(B^1_o)$, $\psi(A^2_o)$, and $\psi(B^2_o)$ of the highest occupied LL is (0, 2, 0, 1). As for the lowest unoccupied LL, it is (2, 1, 2, 0). The spatial symmetry or the oscillating properties of Landau wave functions dominates the feature of optical absorption spectra.

The optical absorption function is given by[35–37]

$$A(\omega) \propto \sum_{\tilde{n},\tilde{n}'} \int_{1\text{stBZ}} \frac{dk_x}{2\pi} \text{Im}\left[\frac{f[E^{c}_{\tilde{n}}(k_x)] - f[E^{v}_{\tilde{n}'}(k_x)]}{E^{c}_{\tilde{n}}(k_x) - E^{v}_{\tilde{n}'}(k_x) - \omega - i\Gamma}\right] \times \left|\left\langle \Phi^{c}_{\tilde{n}}(k_x,y) \left| \frac{\hat{E}\cdot\vec{P}}{m_e} \right| \Phi^{v}_{\tilde{n}'}(k_x,y) \right\rangle\right|^2, \quad (7)$$

where $\tilde{n}$ and $\tilde{n}'$ are subband indices and $f[E_{\tilde{n}}(k_x)]$ is the Fermi-Dirac distribution function. Only the inter-$\pi$-band excitations happen at $T=0$. With an electric polarization $\mathbf{E_x} \| \hat{\mathbf{x}}$, the electromagnetic field excites electrons from the occupied $\pi$ bands ($\tilde{n}' \leq 0$) to the unoccupied $\pi^*$ bands ($\tilde{n} \geq 0$). The optical selection rule is $\Delta k_x = 0$ because of the almost zero momentum of photon.

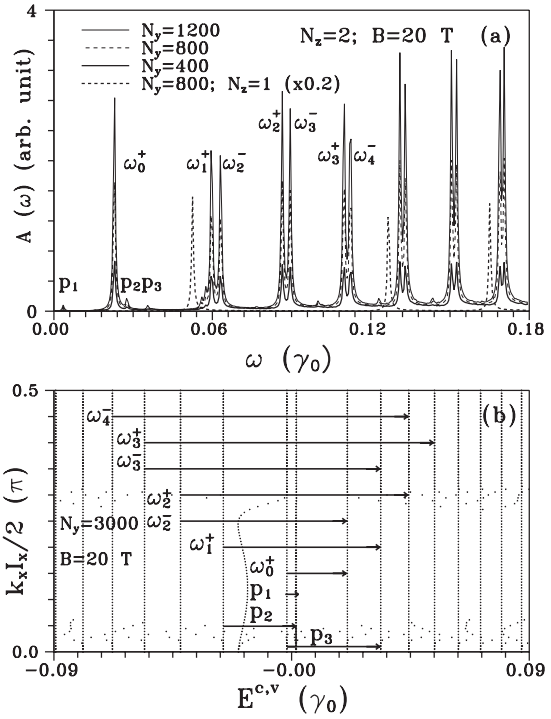


FIG. 4. (a) Magnetoabsorption spectra of bilayer ribbons with various widths at $B=20$ T. Absorption spectrum of the $N_y=800$ monolayer ribbon is also shown. (b) The effective transition channels for the $N_y=3000$ bilayer ribbon at $B=20$ T.

The magnetoabsorption spectra of bilayer graphene ribbons with different ribbon widths at $B=20$ T only exhibit several delta-function-like symmetric peaks [Fig. 4(a)], which come from the transitions between the Landau levels [Fig. 2(b)]. Notably, the frequencies of Landau peaks remain unchanged though the ribbon width grows. They are independent of the ribbon width and deduced to be the same as those of the bilayer graphene. $A(\omega)$'s exhibit stronger peaks for large $N_y$'s, since there are more Landau states and excitation channels. The energy spacings between two neighboring absorption peaks are different. Due to the interlayer interactions, $A(\omega)$ of the $N_y=800$ bilayer graphene ribbon contrast to that of the $N_y=800$ monolayer ribbon in the number, the frequencies, and the energy spacings of the Landau peaks [Fig. 2(a)].

The optical transition channel of each absorption peak could be clearly identified. For instance, the transition channels corresponding to the first seven sharp peaks, denoted as $\omega_0^+, \ldots, \omega_3^+$, and $\omega_4^-$ in Fig. 4(a), are, respectively, indicated in Fig. 4(b). Peaks $\omega_0^+$, $\omega_1^+$, $\omega_2^+$, and $\omega_3^+$ originate in the transitions from the $\tilde{n}'=0$, $-1$, $-2$ and $-3$ subbands to $\tilde{n}=1$, 2, 3 and 4 subbands. As for the Landau peaks $\omega_2^-$, $\omega_3^-$, and $\omega_4^-$, they come from the optical excitations between the $\tilde{n}'=-2$, $-3$, $-4$ subbands and $\tilde{n}=1,2,3$ subbands. The notation $\omega^{\pm}_{\tilde{n}}$ denotes the optical transition between $\tilde{n}'=-\tilde{n}$ subband to $\tilde{n}\pm 1$. That is to say, the selection rule is $\delta|\tilde{n}| = \pm 1$. The optical transition channel and the selection rule are totally determined by the velocity matrix element.

An analytic study is helpful for clarifying the origin of the selection rule $\delta|\tilde{n}| = \pm 1$, which is obtained by the numerical calculation. Based on the gradient approximation, the velocity matrix element $\langle \Phi^c_{\tilde{n}}(k_x,y)|\frac{\hat{E}\cdot\vec{P}}{m_e}|\Phi^v_{\tilde{n}'}(k_x,y)\rangle$ is approximated by $\langle \Phi^c_{\tilde{n}}(k_x,y)|\frac{\partial H}{\partial k_x}|\Phi^v_{\tilde{n}'}(k_x,y)\rangle$. Inserting the tight-binding Bloch functions [Eq. (1)] and Hamiltonian matrix [Eqs. (2) and (3)] into the velocity matrix element, we obtain $\langle \Phi^c_{\tilde{n}}(k_x,y)|\frac{\partial H}{\partial k_x}|\Phi^v_{\tilde{n}'}(k_x,y)\rangle = \Sigma\cdots a^{c*}_{A^1_m}\langle A^1_m|\frac{\partial H}{\partial k_x}|B^1_m\rangle b^v_{B^1_m}\cdots$. Obviously, only the electron jumping from the site $A(B)$ to the nearest neighboring site $B(A)$ can contribute to the velocity matrix element. The following list illustrates the nonzero matrix elements of the representation of operator $\frac{\partial H}{\partial k_x}$:

$$
\begin{aligned}
\left\langle A^1_m \left| \frac{\partial H}{\partial k_x} \right| B^1_m \right\rangle &= -2\gamma_0 I_x \sin\{k_x I_x - \pi(m-[N])\phi\},\\
\left\langle A^1_m \left| \frac{\partial H}{\partial k_x} \right| B^2_m \right\rangle &= -2\gamma_4 I_x \sin\left\{k_x I_x - \pi\left(m-[N]-\frac{1}{3}\right)\phi\right\},\\
\left\langle B^1_m \left| \frac{\partial H}{\partial k_x} \right| A^1_m \right\rangle &= -2\gamma_0 I_x \sin\{k_x I_x - \pi(m-[N])\phi\},\\
\left\langle B^1_m \left| \frac{\partial H}{\partial k_x} \right| A^2_m \right\rangle &= -2\gamma_4 I_x \sin\{k_x I_x - \pi(m-[N])\phi\},\\
\left\langle A^2_m \left| \frac{\partial H}{\partial k_x} \right| B^2_m \right\rangle &= -2\gamma_0 I_x \sin\left\{k_x I_x - \pi\left(m-[N]-\frac{1}{3}\right)\phi\right\},\\
\left\langle A^2_m \left| \frac{\partial H}{\partial k_x} \right| B^1_m \right\rangle &= -2\gamma_4 I_x \sin\{k_x I_x - \pi(m-[N])\phi\},\\
\left\langle B^2_m \left| \frac{\partial H}{\partial k_x} \right| A^2_m \right\rangle &= -2\gamma_0 I_x \sin\left\{k_x I_x - \pi\left(m-[N]-\frac{1}{3}\right)\phi\right\},\\
\left\langle B^2_m \left| \frac{\partial H}{\partial k_x} \right| A^1_m \right\rangle &= -2\gamma_4 I_x \sin\left\{k_x I_x - \pi\left(m-[N]-\frac{1}{3}\right)\phi\right\},\\
\left\langle B^1_m \left| \frac{\partial H}{\partial k_x} \right| B^2_{m+1} \right\rangle &= -2\gamma_3 I_x \sin\left\{k_x I_x - \pi\left(m-[N]+\frac{1}{3}\right)\phi\right\}.
\end{aligned}
\tag{8}
$$

Because of the strong localization of the Landau wave functions, the spatial extent of Landau wave function is so narrow that the phase $\pi(m-[N])\phi$ is negligible, i.e., $\sin\{k_x I_x - \pi(m-[N])\phi\} \approx \sin(k_x I_x)$. Accordingly, the magnitude of velocity matrix element is written as

$$
\begin{aligned}
&\left|\left\langle \Phi^c_{\tilde{n}}(k_x,y)\left|\frac{\partial H}{\partial k_x}\right|\Phi^v_{\tilde{n}'}(k_x,y)\right\rangle\right|\\
&\quad = 2I_x \sin(k_x I_x)\{\gamma_0\langle\Psi^c_{\tilde{n}}(y)|\Psi^v_{\tilde{n}'}(y)\rangle_{\text{intraribbon}}\\
&\quad + (\gamma_4+\gamma_3)\langle\Psi^c_{\tilde{n}}(y)|\Psi^v_{\tilde{n}'}(y)\rangle_{\text{inter-ribbon}}\},
\end{aligned}
\tag{9}
$$

where $\langle\Psi^c_{\tilde{n}}(y)|\Psi^v_{\tilde{n}}(y)\rangle$ is the projection of the envelope function of the initial state on that of the final state. The subscript "intraribbon" ("inter-ribbon") denotes the initial and final states located at the same (different) ribbons. By expanding the envelope function in its associated subenvelope functions, the projections $\langle\Psi^c_{\tilde{n}}(y)|\Psi^v_{\tilde{n}}(y)\rangle_{\text{intraribbon}}$ and $\langle\Psi^c_{\tilde{n}}(y)|\Psi^v_{\tilde{n}}(y)\rangle_{\text{inter-ribbon}}$ are, respectively, expressed as

$$
\begin{aligned}
\langle\Psi^c_{\tilde{n}}(y)|\Psi^v_{\tilde{n}'}(y)\rangle_{\text{intraribbon}} &= \langle\psi^c_{\tilde{n}}(A^1)|\psi^v_{\tilde{n}'-1}(B^1)\rangle\\
&\quad + \langle\psi^c_{\tilde{n}-1}(B^1)|\psi^v_{\tilde{n}'}(A^1)\rangle\\
&\quad + \langle\psi^c_{\tilde{n}}(A^2)|\psi^v_{\tilde{n}'+1}(B^2)\rangle\\
&\quad + \langle\psi^c_{\tilde{n}+1}(B^2)|\psi^v_{\tilde{n}'}(A^2)\rangle\\
&= C_1\delta_{\tilde{n},|\tilde{n}'|-1} + C_2\delta_{\tilde{n},|\tilde{n}'|+1},
\end{aligned}
$$

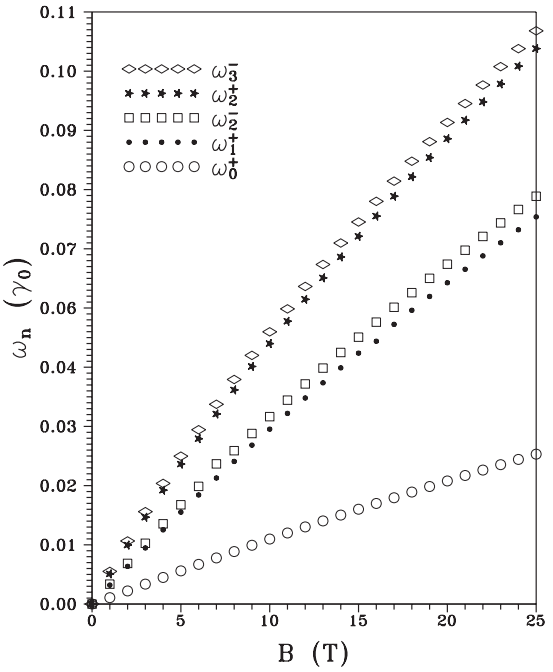


FIG. 5. Frequencies of the first five peaks in the absorption spectra of bilayer ribbon, $\omega_0^+$, $\omega_1^+$, $\omega_2^-$, $\omega_2^+$, and $\omega_3^-$, vs the field strength.

$$\begin{aligned}\langle \Psi_{\tilde{n}}^{c}(y)|\Psi_{\tilde{n}'}^{v}(y)\rangle_{\text{inter-ribbon}} &= \langle \psi_{\tilde{n}}^{c}(A^1)|\psi_{\tilde{n}'+1}^{v}(B^2)\rangle \\ &+ \langle \psi_{\tilde{n}-1}^{c}(B^1)|\psi_{\tilde{n}'}^{v}(A^2)\rangle \\ &+ \langle \psi_{\tilde{n}}^{c}(A^2)|\psi_{\tilde{n}'-1}^{v}(B^1)\rangle \\ &+ \langle \psi_{\tilde{n}+1}^{c}(B^2)|\psi_{\tilde{n}'}^{v}(A^1)\rangle \\ &= D_1\delta_{\tilde{n},|\tilde{n}'|-1} + D_2\delta_{\tilde{n},|\tilde{n}'|+1}. \quad (10)\end{aligned}$$

Finally, the velocity matrix element $\langle \Phi_{\tilde{n}}^{c}(k_x,y)|\frac{\hat{E}\cdot\vec{P}}{m_e}|\Phi_{\tilde{n}'}^{v}(k_x,y)\rangle$ is equal to $-2I_x \sin(k_x I_x)\{[\gamma_0 C_1+(\gamma_4+\gamma_3)D_1]\delta_{\tilde{n},|\tilde{n}'|-1}+[\gamma_0 C_2+(\gamma_4+\gamma_3)D_2]\delta_{\tilde{n},|\tilde{n}'|+1}\}$, which determines the selection rule $|\tilde{n}'|-\tilde{n}=\pm 1$ and the effective transition channels.

In addition to the sharp Landau peaks, there are several small bumps, $P_1$, $P_2$, and $P_3$ in the absorption spectra, for example. Their transition channels are also identified and shown in Fig. 4(b). The first peak $P_1$ results form the transition between the highest occupied state ($\tilde{n}'=0$) and the lowest unoccupied state ($\tilde{n}=0$). The absorption frequency of $P_1$ is equal to the size of band gap $E_g$. The projection $\langle \psi^c(B^2)|\psi^v(A^2)\rangle$ contributes to the velocity matrix element and gives rise to this small bump. $P_2$ peak originates in the transition between the $\tilde{n}'=-1$ and $\tilde{n}=0$ levels. The projection $\langle \psi^c(B^1)|\psi^v(A^1)\rangle$ leads to this peak. The transition between $\tilde{n}'=0$ and $\tilde{n}=2$ leads to the $P_3$ peak.

The $B$-dependent absorption frequencies of Landau peaks are helpful in understanding the characteristics of the magnetoabsorption spectra. The absorption frequencies of the first five peaks of the bilayer ribbon, $\omega_0^+$, $\omega_1^+$, $\omega_2^-$, $\omega_2^+$, and $\omega_3^-$, are shown in Fig. 5. $\omega$'s make a blue shift as the field strength increases. In the energy region $\omega<0.04\gamma_0 \approx 100$ meV, all absorption frequencies of Landau peaks are linear in $B$. The absorption frequency of the first Landau peak $\omega_0^+$ is linearly dependent on field strength even when the testing $B$ field is up to 25 T. The chief reason is that $\omega_0^+$ results from the transition between the $\tilde{n}'=0$ occupied state and the $\tilde{n}=1$ occupied state. The state energies of the initial and final states both follow the $E^{c,v}\propto B$ relation at $B\leq 25$ T [Fig. 2(c)]. This leads to the linear $B$-dependent $\omega_0^+$. On the other hand, $\omega_1^+$, $\omega_2^-$, $\omega_2^+$, and $\omega_3^-$ exhibit a different $B$-dependence behavior. They are linear functions of the field strength at $B\leq 5$ T while they show the $\omega\propto\sqrt{B}$ relation at $B\geq 20$ T. At $B\leq 5$ T, the initial and final states of $\omega_1^+$, $\omega_2^-$, $\omega_2^+$, or $\omega_3^-$ observe the $E^{c,v}\propto B$ relation [the inset of Fig. 2(c)]. Such a linear-in-$B$ dependence is missing when the field strength increases. At $B\geq 20$ T, both the initial and final states of the optical excitation abide by the simple relation $E_{\tilde{n}}^{c}(E_{\tilde{n}'}^{v})\propto\sqrt{B}$ [Fig. 2(d)]. As a result, $\omega$'s show linear-in-$\sqrt{B}$ dependence.

A comparison is made between literatures and the present work, exploring the magnetoabsorption spectra of an unbiased bilayer graphene ribbon. The optical property of biased bilayer graphene in the presence of **B** is studied.[18] A four-band continuum model is employed to analytically study the Landau-level energies and the related wave functions. The effects caused by the interlayer interactions, the strength of gated field, and the magnitude of magnetic field are taken into consideration. The oscillator strength for electric dipole transitions between the Landau states, namely the velocity matrix element in this work, is then calculated. The selection rule associated with the interband or intraband transition follows $|\tilde{n}'|-|\tilde{n}|=\pm 1$, which is the same as that of the present work. In contrast to an unbiased system, Ref. 18 shows that the interband transitions of a biased bilayer are significantly shifted in energy due to the opening of an energy gap caused by the gated field, and electric-field-modulated oscillator strength exhibits $B$-field dependence. Such interesting properties result from the cooperation of interlayer interactions, magnetic field, and gated field. In the absence of external fields, the interlayer interactions change the two pairs of the linear bands to four complicated bands. Each band consists of parabolic bands and sublinear bands.[10–13] The application of **B** field induces the Landau levels (flatbands) and related Landau wave functions. The gated field produces a potential difference $\Delta U$ between the two graphene layers. It chiefly shifts the Landau-level energies and modifies the characteristic of wave functions. As a result, gated field changes the transition energy of interband excitation and the corresponding oscillator strength. Through the destruction of the degeneracy between two layers, the gated field can open a band gap in the absence or presence of **B**. Such an effect is different from that caused by the chemical difference $\gamma_6$. In this work, $\gamma_6$ makes a contribution to the opening of a band gap in the presence of **B**. Moreover $\gamma_6$ destroys the degeneracy between $A$ and $B$ atoms through the changes of the site energy of $A$ atom. On the other hand, anomalous absorption line in magnetoabsorption spectra of a monolayer graphene with or without an excitonic gap is theoretically studied.[38,39] The frequencies and intensities of absorption lines in quite low energy region vary with the chemical potential, which can be experimentally tunable by the application of gate bias

voltage to a field effect device. We are so inspired by the interesting properties mentioned above[18,24,38] to further study the magnetoabsorption spectra of a bilayer graphene (ribbons).

## IV. CONCLUSIONS

The Peierls-coupling tight-binding method is employed to study the low-energy magnetoabsorption spectra of the AB-stacked bilayer graphene ribbons. Absorption spectra exhibit several sharp Landau peaks, which are strongly affected by the interlayer interactions and magnetic-field magnitude. Because of the inter-ribbon interactions, $A(\omega)$ of the bilayer graphene ribbon contrasts with that of the monolayer ribbon in the number, the frequencies, and the energy spacings of the Landau peaks. Moreover, magnetoabsorption spectra exhibit denser Landau peaks in a bilayer ribbon than in a monolayer ribbon. The absorption frequencies of Landau peaks of the bilayer ribbon do not follow the simple relation $\omega \propto \sqrt{B}$. The findings show that the frequency of the first peak is linearly proportional to field strength even though the field strength up to $B=25$ T. Other peaks show the $B$-dependence frequencies at $B \leq 5$ T and the $\sqrt{B}$-dependence frequencies at $B \geq 16$ T. The interesting magnetoabsorption spectra result from the magnetoelectronic properties. As a result of the interlayer interactions, the magnetic energy bands of a bilayer graphene ribbon are different from those of a monolayer ribbon in the Landau-level energies, the energy spacing, the state degeneracy, and the number of the Landau levels. The interlayer interactions also induce a band gap and cause denser Landau levels. In the energy region $|E| \leq 50$ meV, the Landau-level energies follow the relation $|E| \propto \tilde{n}B$. At $|E| \geq 50$ meV, even a simple relation between $E$ and $\tilde{n}$ could not be figured out. The Landau plot shows that Landau levels grow with **B** at a low field $B \leq 5$ T, whereas they are $\sqrt{B}$ dependent at the field strength $B \geq 20$ T. The properties of Landau wave functions are also explored. They contribute to understand the transition channels of the Landau peaks and the optical selection rule $\Delta\tilde{n} = \pm 1$. Most important of all, the predicted results could be verified by the optical measurements, and the findings lead to an access to the magnetoelectronic properties and the optical spectra of a 2D bilayer graphene.

## ACKNOWLEDGMENTS

This work was supported by the Taiwan National Science Council (Grants No. NSC 96-2112-M-165-001-MY3 and NSC 95-2112-M-006-0002).

*t00252@mail.tut.edu.tw
†mflin@mail.ncku.edu.tw

[1] K. S. Novoselov, A. K. Geim, S. V. Morozov, D. Jiang, Y. Zhang, S. V. Dubonos, I. V. Grigorieva, and A. A. Firsov, Science **306**, 666 (2004).
[2] J. S. Bunch, Y. Yaish, M. Brink, K. Bolotin, and P. L. McEuen, Nano Lett. **5**, 287 (2005).
[3] Y. B. Zhang, J. P. Small, M. E. S. Amori, and P. Kim, Phys. Rev. Lett. **94**, 176803 (2005).
[4] Y. H. Wu, B. J. Yang, B. Y. Zong, H. Sun, Z. X. Shen, and Y. P. Feng, J. Math. Chem. **14**, 469 (2004).
[5] A. K. Geim and K. S. Novoselov, Nat. Mater. **6**, 183 (2007).
[6] D. V. Khveshchenko, Phys. Rev. Lett. **87**, 246802 (2001).
[7] K. S. Novoselov, A. K. Geim, S. V. Morozov, D. Jiang, M. I. Katsnelson, I. V. Grigorieva, S. V. Dubonos, and A. A. Firsov, Nature (London) **438**, 197 (2005).
[8] Y. Zhang, Y. W. Tan, H. L. Stormer, and P. Kim, Nature (London) **438**, 201 (2005).
[9] V. P. Gusynin and S. G. Sharapov, Phys. Rev. Lett. **95**, 146801 (2005).
[10] S. Latil and L. Henrard, Phys. Rev. Lett. **97**, 036803 (2006).
[11] M. Aoki and H. Amawashi, Solid State Commun. **142**, 123 (2007).
[12] C. L. Lu, C. P. Chang, Y. C. Huang, J. H. Ho, C. C. Hwang, and M. F. Lin, J. Phys. Soc. Jpn. **76**, 024701 (2007).
[13] E. V. Castro, K. S. Novoselov, S. V. Morozov, N. M. R. Peres, J. M. B. Lopes dos Santos, J. Nilsson, F. Guinea, A. K. Geim, and A. H. Castro Neto, Phys. Rev. Lett. **99**, 216802 (2007).
[14] C. L. Lu, C. P. Chang, Y. C. Huang, R. B. Chen, and M. L. Lin, Phys. Rev. B **73**, 144427 (2006).
[15] T. Ohta, A. Bostwick, T. Seyller, K. Horn, and E. Rotenberg, Science **313**, 951 (2006).
[16] E. McCann and V. I. Fal'ko, Phys. Rev. Lett. **96**, 086805 (2006).
[17] D. S. L. Abergel and V. I. Fal'ko, Phys. Rev. B **75**, 155430 (2007).
[18] J. M. Pereira, F. M. Peeters, and P. Vasilopoulos, Phys. Rev. B **76**, 115419 (2007).
[19] P. Fekete and G. Gumbs, J. Phys.: Condens. Matter **11**, 5475 (1999).
[20] T. B. Boykin and P. Vogl, Phys. Rev. B **65**, 035202 (2001).
[21] C. P. Chang, C. L. Lu, Y. K. Fang, R. B. Chen, F. L. Shyu, and M. F. Lin, Carbon **42**, 2975 (2004).
[22] C. P. Chang, C. L. Lu, F. L. Shyu, R. B. Chen, Y. C. Huang, and M. F. Lin, Carbon **43**, 1424 (2005).
[23] N. Nemec and G. Cuniberti, Phys. Rev. B **74**, 165411 (2006).
[24] N. Nemec and G. Cuniberti, Phys. Rev. B **75**, 201404(R) (2007).
[25] Y. H. Lai, J. H. Ho, C. P. Chang, and M. F. Lin, Phys. Rev. B **77**, 085426 (2008).
[26] Y. C. Huang, C. P. Chang, and M. F. Lin, J. Appl. Phys. **103**, 073709 (2008).
[27] Y. C. Huang, C. P. Chang, and M. F. Lin, Nanotechnology **18**, 495401 (2007).
[28] L. Brey and H. A. Fertig, Phys. Rev. B **73**, 235411 (2006); **73**, 195408 (2006).
[29] J. C. Charlier, X. Gonze, and J. P. Michenaud, Phys. Rev. B **43**, 4579 (1991).
[30] C. T. White, J. W. Li, D. Gunlycke, and J. W. Mintmire, Nano Lett. **7**, 825 (2007).
[31] Y. Miyamoto, K. Nakada, and M. Fujita, Phys. Rev. B **59**, 9858 (1999).

[32] A. H. MacDonald, Phys. Rev. B **29**, 6563 (1984).
[33] Y. Hatsugai, Phys. Rev. B **48**, 11851 (1993).
[34] E. A. Henriksen, Z. Jiang, L.-C. Tung, M. E. Schwartz, M. Takita, Y.-J. Wang, P. Kim, and H. L. Stormer, Phys. Rev. Lett. **100**, 087403 (2008).
[35] C. P. Chang, Y. C. Huang, C. L. Lu, J. H. Ho, T. S. Li, and M. F. Lin, Carbon **44**, 508 (2006).
[36] J. G. Johnson and G. Dresselhaus, Phys. Rev. B **7**, 2275 (1973).
[37] M. F. Lin and Kenneth W.-K. Shung, Phys. Rev. B **50**, 17744 (1994).
[38] V. P. Gusynin, S. G. Sharapov, and J. P. Carbotte, Phys. Rev. Lett. **98**, 157402 (2007).
[39] V. P. Gusynin, S. G. Sharapov, and J. P. Carbotte, J. Phys.: Condens. Matter **19**, 026222 (2007).